A simple step heating approach for wall surface temperature estimation in the SOlar and LongWave Environmental Irradiance Geometry (SOLWEIG) model

Nils Wallenberg[1], Björn Holmer[1], Fredrik Lindberg[1], Jessika Lönn[1], Erik Maesel[1], David Rayner[2]

[1]Department of Earth Sciences, University of Gothenburg, Gothenburg, Medicinaregatan 7B, 413 90 Göteborg, Sweden

[2]Swedish National Data Service, University of Gothenburg, Gothenburg, Medicinaregatan 18A, 413 90 Göteborg, Sweden

Correspondence to: Nils Wallenberg (nils.wallenberg@gvc.gu.se)

Abstract. The urban climate is highly influenced by its building geometry, material characteristics, street orientation and high fraction of impermeable surfaces. All of these influence the microclimate and the resulting outdoor thermal comfort. Mean radiant temperature (T_{mrt}) is often used as an estimator for heat exposure as it is one of the most important variables governing outdoor human thermal comfort on clear, calm and warm days. The highest values of T_{mrt} are commonly found in front of sunlit facades where a human is exposed to high levels of direct and reflected shortwave radiation from the sun, as well as high levels of longwave radiation emitted from surrounding sunlit walls. As a consequence, outdoor thermal comfort modelling requires accurate simulation of wall surface temperatures (T_s).

The aim of this study is to present a step heating approach for calculating wall T_s in the SOlar and LongWave Environmental Irradiance Geometry model (SOLWEIG) and quantifying how it influences T_{mrt}. This method requires information on material characteristics, i.e. specific heat capacity, density, thermal conductivity, albedo and thickness of the outer layer of the wall, as well as radiation balance at the wall surface, and ambient air temperature. Simulated T_s is compared to observed T_s of two white walls (albedo = 0.5) in Gothenburg, Sweden; one wooden wall and one plaster brick wall. The simulations show high agreement with the 15,394 observations, with R^2 = 0.93 and RMSE = 2.09 °C for the wooden wall and R^2 = 0.94 and RMSE = 1.94 °C for the plaster brick wall. For the walls presented here, this new parameterization scheme results in differences in T_{mrt} of up to 2.5 °C compared to the previous version of SOLWEIG.

With this new approach SOLWEIG can be used to evaluate the effect of building materials on outdoor thermal comfort. The speed and accuracy of this approach suggests that it also could be applied in other areas where T_s of walls are important, for example building energy models and urban energy balance models.

1 Introduction

The climate in urban areas is highly influenced by its building geometry (Muniz-Gäal et al., 2020; Nasrollahi et al., 2021; Xi et al., 2021), the orientation of streets (Ali-Toudert & Mayer, 2005), material characteristics (Santamouris and Yun, 2020; Adilkhanova et al., 2023; Battista et al., 2023), vegetation (Schibuola, L. & Tambani, C, 2022; Stache et al., 2022) and the relatively high fraction of impermeable surfaces (Arnfield, 2003). Outdoor human thermal comfort is a consequence of the resulting microclimate. On clear, calm and warm days,

the mean radiant temperature (T_{mrt}) is one of the most important factors in describing the outdoor thermal comfort of a human, and is used in many thermal comfort indices, e.g. the Physiological Equivalent Temperature (PET) (Höppe et al., 1999) and the Universal Thermal Climate Index (UTCI) (Blazejczyk et al., 2010). T_{mrt} describes

40   the radiant load that a human is exposed to, i.e. the exchange of short- and longwave radiation between the person and its surrounding radiative environment (Höppe, 1992; Thorsson et al., 2007). While spatial differences in air temperature (T_{air}) are usually very small in Nordic urban environments, the spatial differences in T_{mrt} between sunlit and shaded spaces can be up to 30 °C (Lau et al., 2015). For these reasons, many authors stress the importance of accurate modeling of T_{mrt} (Di Napoli et al., 2020; Gál and Kántor, 2020).

45   The shortwave radiation that a human is exposed to originates from the sun, with direct, diffuse and reflected components, whereas the longwave radiation originates from the sky, ground, vegetation and building surfaces, e.g. walls. There are numerous models to calculate T_{mrt}, including ENVI-met (Bruse and Fleer, 1998), RayMan (Matzarakis et al. 2007; Matzarakis et al. 2010), PALM-4U (Maronga et al., 2020) and The SOlar and LongWave Environmental Irradiance Geometry model (SOLWEIG) (Lindberg et al., 2008), all of which to some extent

50   handle the above mentioned fluxes. Highest values of T_{mrt} are commonly found in front of sunlit walls (Lindberg et al., 2014) because this is where a person would be exposed to direct and diffuse shortwave radiation as well as comparatively high amounts of reflected shortwave radiation off the wall (Wallenberg et al., 2020). Another highly influential aspect is if the wall is (or has recently been) sunlit, which increases its surface temperature (T_s) so that a person located close to the wall is exposed to higher emittance of longwave radiation.

55   There are several ways of estimating the T_s of a material. A common approach is with Fourier's law of diffusion (e.g. Simon, 2016; Resler et al., 2017), where the T_s of a material is calculated based on its energy balance that is estimated from heat conduction to or from the interior of the material, convection and radiative exposure. Here, thermal properties such as thermal conductivity, specific heat capacity and emissivity of the material are important, information that is not always easily accessible, especially in the interior of the walls. While this

60   approach is accurate and dynamical, it is relatively time-consuming. Other approaches include empirical relationships, where T_s is observed and related to environmental variables, e.g. T_{air} or solar radiation, as in Bogren et al. (2000) and Lindberg et al. (2016). The empirical approach is only accurate for the specific material that it is calibrated on and requires logistically demanding field observations to incorporate new materials in modeling. A third approach that can be used to estimate the T_s of a material is step heating. Boue & Fournier (2009) used a

65   step heating equation derived from the Dirac heat pulse to estimate T_s of materials. This is a straightforward approach, where the radiation balance at the surface of the material is used together with its thermal effusivity. Here, thermal effusivity describes the ability of a material to absorb or return the thermal energy at its surface, for example between a wall surface and the ambient air.

A common approach to estimate T_s of walls is to divide it into several layers and calculate its energy balance

70   based on Fourier's law of diffusion. The ENVI-met model uses three layers and calculates the temperature in seven nodes (Simon, 2016), whereas PALM-4U uses four layers and six nodes (Resler et al., 2017; 2021). Both of these models can simulate T_s with high accuracy. Up to now, the SOLWEIG model uses the empirical approach described in Bogren et al. (2000) and Lindberg et al (2016). The simulated T_s of ENVI-met (Simon, 2016) and PALM-4U (Resler et al., 2017; 2021) show high agreement with observations. The T_s of walls simulated with

75   SOLWEIG has not been evaluated specifically. Gal & Kantor (2020) found that T_{mrt} simulated with SOLWEIG

was underestimated in sunlit areas and overestimated in shaded areas, and that these offsets could be related to its wall surface temperature parameterization. Wallenberg et al. (2023) also argued that the parameterization of wall surface temperatures in SOLWEIG could result in deviations in simulated emitted longwave radiation from building surfaces.

80   The aim of this study is to present and evaluate a new step heating model approach for calculations of T_s of walls in the SOLWEIG model, and how this affects the microclimate and T_{mrt}.

2 Methods

2.1 Surface temperature parameterization

The basis of the T_s simulation is the step heating equation derived from the Dirac heat pulse as described in e.g.
85   Boue & Fournier (2009):

$$T_s = \frac{2\omega}{e}\sqrt{\frac{t}{\pi}} + T_{air} \tag{1}$$

where:

- ω is the heat flux density (W/m^2), i.e. the sum of incoming and outgoing short- and longwave radiation of the wall;

90   - e is the thermal effusivity (W s$^{0.5}$ m^{-2} K^{-1}) of the wall surface material, derived from:

$$e = \sqrt{\lambda \rho C} \tag{2}$$

with λ being the thermal conductivity of the material, ρ is the density and C is the specific heat capacity.

- t is the characteristic time in seconds, as described below.
- T_{air} is the air temperature.

95   The wall surface is considered a semi-infinite solid that has a thickness L and extends infinitely in other directions. The time t in eq. 1 is estimated from the characteristic time that describes the time it takes for the energy to propagate from the outdoor surface of the material to its interior end, i.e. through the thickness L. The characteristic time is calculated according to eq. 3 (Parker et al., 1961; Cape & Lehman, 1963; Xue et al., 1993; Philipp et al., 2019):

100
$$t = \frac{L^2}{(\pi^2 \kappa)} \tag{3}$$

where κ is the thermal diffusivity calculated from $\lambda / \rho C$.

The initial T_s at timestep 0 is set to T_{air} and the simulation should therefore ideally start at nighttime when $T_s \approx T_{air}$. After this, T_s at timestep i is set to $T_{s,i-1}$ and T_{air} is $T_{air,i}$.

2.2 Calculation of received short- and longwave radiation

105   ω (in eq. 1) is the sum of incoming and outgoing short- and longwave radiation for the wall surface of interest. It is calculated here with the SOLWEIG model (Lindberg et al., 2008) that is described in more detail in section 2.4.

2.2.1 Shortwave radiation

The shortwave radiation is the sum of the direct (K_{dir}), sky diffuse (K_{diff}) and reflected (K_{ref}) components. These components are calculated as follows:

$$K_{dir} = (1 - \alpha_{wall}) \times I \times Sh \times \zeta \tag{4}$$

$$K_{diff} = (1 - \alpha_{wall}) \times D \times \psi \tag{5}$$

$$K_{ref} = (1 - \alpha_{wall}) \times \left(G \times \alpha_{wall} \times F_b + G \times \alpha_g \times F_g\right) \tag{6}$$

where I is the direct shortwave radiation from the sun, D is the sky diffuse shortwave radiation and G is horizontal global radiation. α_{wall} and α_g are the albedo of the wall and ground surface respectively, Sh is a Boolean value

115   indicating if the wall surface is sunlit or not, ζ is the angle of incidence (defined below) of I and ψ is the sky view factor at the wall surface. K_{ref} consists of two terms, where the first one refers to shortwave radiation reflected off surrounding buildings surfaces (F_b, defined below) and the second refers to shortwave radiation reflected off the ground (F_g, defined below).

The angle of incidence, ζ, is calculated according to eq. 7:

$$\zeta = \cos\eta \cos\theta \cos\varphi + \sin\eta \sin\theta \sin\varphi \tag{7}$$

Where η is the solar altitude, θ is the solar azimuth and φ is the wall aspect (0° = north facing wall).

2.2.2 Longwave radiation

The longwave radiation is the sum of longwave radiation from surrounding sunlit walls ($L_{wall,sun}$), surrounding shaded walls ($L_{wall,sh}$), the sky (L_{sky}), reflected (L_{ref}) and ground (L_{ground}) and are calculated according to equations:

$$L_{wall,sun} = \sigma \varepsilon_w T_{s,sun}^4 F_b (1 - f_{sh}) f_{sun} \tag{8}$$

$$L_{wall,sh} = \sigma \varepsilon_w T_{s,sh}^4 F_b (1 - f_{sh})(1 - f_{sun}) + \sigma \varepsilon_w T_{s,sh}^4 F_b f_{sh} \tag{9}$$

$$L_{sky} = \sigma \varepsilon_{sky} T_{air}^4 \psi \tag{10}$$

$$L_{ref} = (1 - \varepsilon_w)\left(L_{down} + L_{up}\right)F_b \tag{11}$$

$$L_{ground} = L_{up} F_g \tag{12}$$

130   where σ is Stefan-Boltzmann constant, ε_w and ε_{sky} (calculated here according to Prata 1996) are the emissivity of the wall and sky respectively, $T_{s,sun}$ and $T_{s,sh}$ are the mean surface temperature of the model domain sunlit and shaded wall surfaces respectively, F_b is the fraction of non-sky surfaces, f_{sh} is the sunlit fraction calculated as from a cylindric wedge (Lindberg et al., 2008) and f_{sun} is the fraction of sunlit non-sky surfaces. L_{up} is calculated according to equation 17 in Lindberg et al (2016) and L_{down} according to equation 15 in Wallenberg et al. (2023a).

135 The fraction of non-sky surfaces, f_{sun}, is calculated based on the wall aspect and solar azimuth and is scaled between 0.2 and 0.8:

$$f_{sun} = 0.2 + \frac{|\varphi - \theta|}{180°} \times 0.6 \qquad (13)$$

The scaling is performed to avoid totally sunlit or totally shaded areas. It is reasonable to assume that a built-up area facing the sun is not totally sunlit but would consist of partly shaded areas.

140 An outgoing longwave component is also calculated based on the wall T_s of the previous timestep (i-1):

$$L_{out} = \varepsilon_w \sigma T_s^4 \qquad (14)$$

2.3 Spatial calculation of voxel locations

Individual vertical pixels are described as voxels. The spatial calculation of where each voxel is located is realized at the same spatial resolution as for ground pixels. The locality is determined with the shadow casting algorithm

145 in SOLWEIG (Ratti & Richens, 1999).

To determine which voxel is visible from which ground pixel the patch methodology presented in Wallenberg et al. (2020; 2023) is utilized. SVF (Ψ) used in equations 5 and 10 is calculated at each voxel height and can never exceed 0.5 as only half of the hemisphere is seen. The fraction of buildings (F_b) is:

$$F_b = 1 - \psi_g - 0.5 \qquad (15)$$

150 where ψ_g is SVF at ground level. At ground level it can be assumed that 0.5 of what is seen by a voxel is ground surface. For example, if ψ_g is 0.25 and ground seen is 0.5, the remaining fraction, F_b = 0.25, is non-sky. Fraction of vegetation is calculated in a similar way:

$$F_v = 1 - \psi_v - 0.5 \qquad (16)$$

If F_b and F_v are assumed to not change with height, the ground fraction (F_g) seen by voxels at higher levels is then:

155
$$F_g = 1 - F_v - F_b - \psi \qquad (17)$$

where F_g is expected to change with a change in ψ, i.e. SVF at each voxel.

2.4 SOLWEIG simulation setup

SOLWEIG is a 2.5D radiation model commonly used in studies on radiant load of humans (e.g. Thom et al., 2016; Bäcklin et al., 2021; Wallenberg et al., 2023b). The model is available in the Universal Multi-scale Environmental

160 Predictor (UMEP) (Lindberg et al., 2018). Radiant conditions are estimated in SOLWEIG from pixel-based information on ground and building elevation (Digital Surface Model (DSM)) together with meteorological data (at least global shortwave radiation, T_{air} and relative humidity). Optionally, it is also possible to include pixel-based information on vegetation height (Canopy Digital Surface Model (CDSM)) as well as ground cover. The shadow casting algorithm in SOLWEIG (Ratti and Richens, 2004; Lindberg and Grimmond, 2010; 2011) utilizes

165 the information on elevation of ground, buildings and vegetation to calculate shadows, including shadows on

walls, thus differentiating between shaded and sunlit pixels. SOLWEIG has been evaluated in several studies (e.g. Lindberg et al., 2008; Lindberg and Grimmond, 2011; Kantor et al., 2018; Gal and Kantor, 2020).

Here, we use DSM and CDSM at 0.5 m spatial resolution (81x80 pixels), with walls divided into 0.5 m voxels, together with direct and diffuse shortwave radiation, T_{air}, relative humidity and mean sea level pressure at 10-

170 minute temporal resolution to calculate the net radiation balance ω of the wall surfaces. The walls have been divided into 7182 unique voxels. T_{air} and relative humidity was observed with a TinyTag Plus 2 (Tinytag, 2019) located on the northern side of the building (see Section 2.5). The remaining meteorological variables were retrieved from a weather station on the rooftop of the Department of Earth Sciences, University of Gothenburg (57.6883°, 11.9663°).

175 **2.5 Field observations**

Observations were conducted on a three-storey building in Gothenburg, Sweden. The wall is built of two different materials, where the ground floor consists of plastered brick ($L = 0.1$ m) while the upper two are made of wood ($L = 0.03$ m) (Fig. 1). Both parts of the wall are painted white. They have the same aspect but differ due to the different height and SVF and thus in incoming short and longwave radiation. The observations were conducted

180 with two Apogee SI-111 Research-Grade Standard Field of View Infrared Radiometer Sensors (Apogee Instruments, 2024) positioned approximately 10 cm from the wall surfaces. All wall characteristics except for the albedo and emissivity are set according to look-up tables (CIBSE (2015) and are presented in Table 1. Observations lasted from 2023-05-15 to 2023-08-31, thus covering an entire summer with varying weather from entirely clear days (e.g. 12th of June) to fully overcast (e.g. 8th of August). Ambient T_{air} ranged from 5.7 °C (17th

185 of May 8:20) to 28.4 °C (17th of June 11:30) and daily average shortwave radiation ranged from 24 Wm[-2] to 375 Wm[-2]. Albedo of the walls was assumed to be 0.5 (see e.g. Celniker et al., 2021 for albedos of similar walls). The wall emissivity was set to 0.95 to match the settings of the Apogee SI-111 sensor.

Table 1: Thermal conductivity (λ), density (ρ), specific heat capacity (C), thermal diffusivity (κ) and thermal effusivity (e) of the materials studied. Values for κ and e are calculated based on λ, ρ and C retrieved from CIBSE (2015) (tables

190 **[1]3.37, [2]3.38 and [3]3.46).**

Wall type	λ (W m^{-1} K^{-1})	ρ (kg -m[-3])	C (J kg^{-1} K^{-1})	κ (m[2] s^{-1} 10^{-6})	e (J m^{-2} s[-0.5] K^{-1})
Brick, outer leaf[1]	0.84	1700	800	0.62	1068
Dense plaster[3] (on brick)	0.57	1300	1000	0.44	860
Hardwood (unspecified), dry[2]	0.17	700	1880	0.13	472
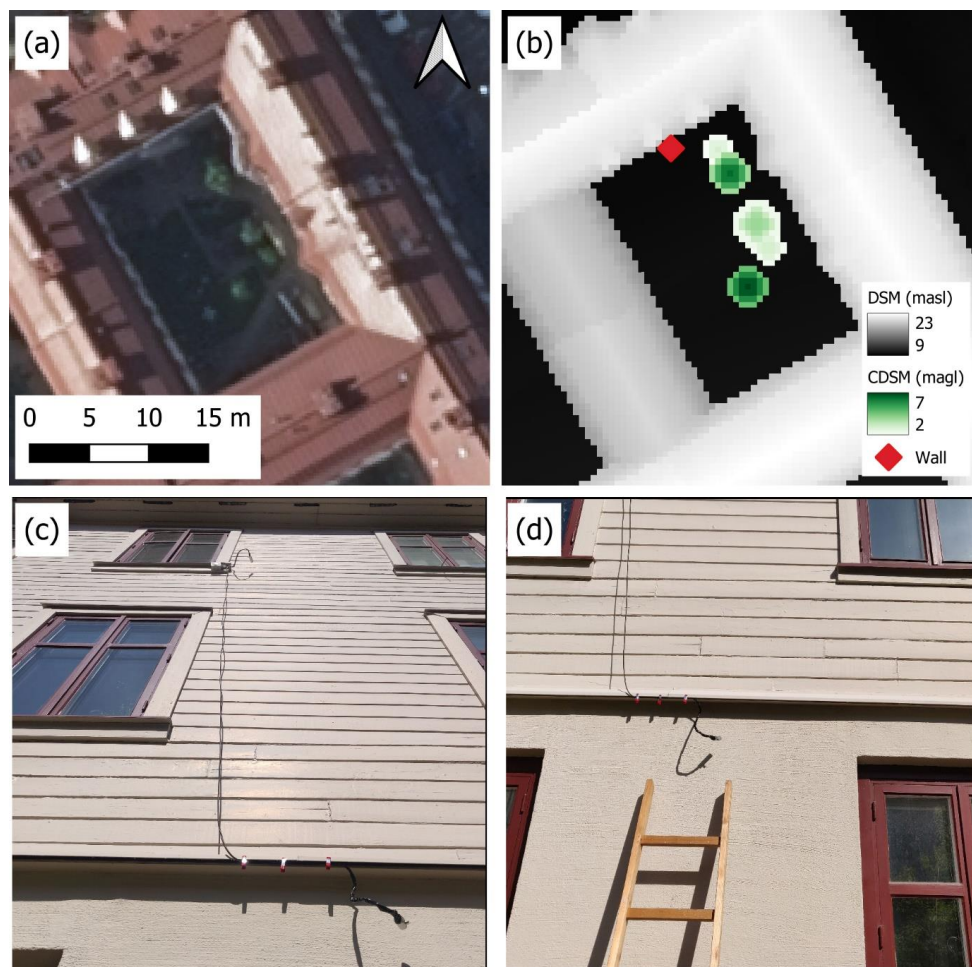
Figure 1: Orthophoto (© Lantmäteriet) (a) and digital surface model (DSM) and canopy digital surface model (CDSM) (b) of the courtyard surrounding the observed wall. The location of the wall is indicated by a red diamond. The observed walls with sensors can be seen in (c) and (d).

3 Results

Five days of simulated and observed wall T_s for the wooden and plaster brick walls are presented in figure 2a and 2b, respectively. These days are characterized by relatively high T_{air}, peaking at between 22-26 °C (figure 2c), and mainly clear weather conditions, with $K_\downarrow$ at solar noon peaking at 860-914 Wm^{-2} (figure 2c). Both walls show good agreement, with the simulated wall T_s consistently following the observed values. However, some deviations are evident, particularly around the time the wall becomes sunlit and in the nighttime. Around sunrise the simulated T_s for the wooden wall are underestimated at 2-6 °C (figure 2a). In the afternoon the simulated cooling rate of the wall is too slow, leading to overestimations of around 1-2 °C that continue into the nighttime. For the last two days, midday temperatures were underestimated by around 5 °C.

The simulated T_s for the plaster brick wall (figure 2b) overestimate up to 2 °C at midday during the first three days. Contrary to the wooden wall, the plaster brick wall underestimates from the evening into nighttime, with 1-3 °C, as an effect of a too rapid simulated cooling rate.
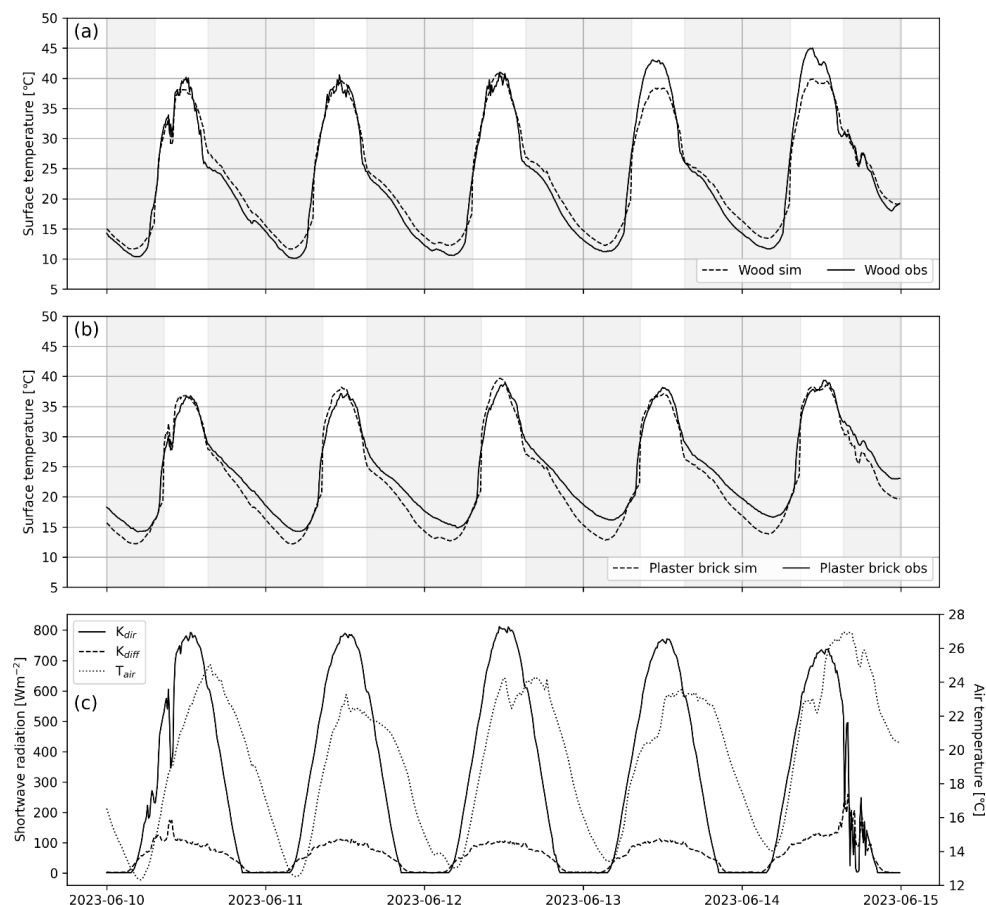
Figure 2: Plots showing five days of observed (solid) and simulated (dashed) wall surface temperature in 10-minute temporal resolution for (a) the wooden wall and (b) the plaster brick wall. Grey areas show when the wall voxel is in simulated shade. Meteorological forcing data is given in (c), with direct solar radiation (K_{dir}) in solid, diffuse solar radiation (K_{diff}) in dashed and air temperature (T_{air}) in dotted lines.

Fig. 3 shows the diurnal development for the whole study period (2023-05-15 – 2023-08-31). The top panel (figure 3a) shows T_s for the wooden wall. The mean values of the simulation (dashed blue line) are aligned with the mean of the observations (solid line), with a small underestimation of 1-2 °C between 08:00-13:00. Before and after these hours, simulations are close to observations with a very small overestimation. The spread of the data can be explained by different weather conditions, ranging from fully overcast, shown as low daytime values, to high values correlating to clear weather conditions with high amounts of incoming solar radiation. Here, it is also noticeable that the simulations (in blue) diverge from the observations, with underestimations during intense solar radiation and overestimations in nighttime.

The plaster brick wall, presented in figure 3b, shows opposite patterns compared to the wooden wall. Here, simulations overestimate with 1 °C in daytime, and underestimates with around 2-3 °C in nighttime. These patterns are also visible in the spread of the data, where simulations overestimate intense solar radiation. There is a narrower spread for the plaster brick wall, compared to the wooden wall, which can be explained by their material characteristics, i.e. the wooden wall reacts much faster to changes in solar radiation.

225
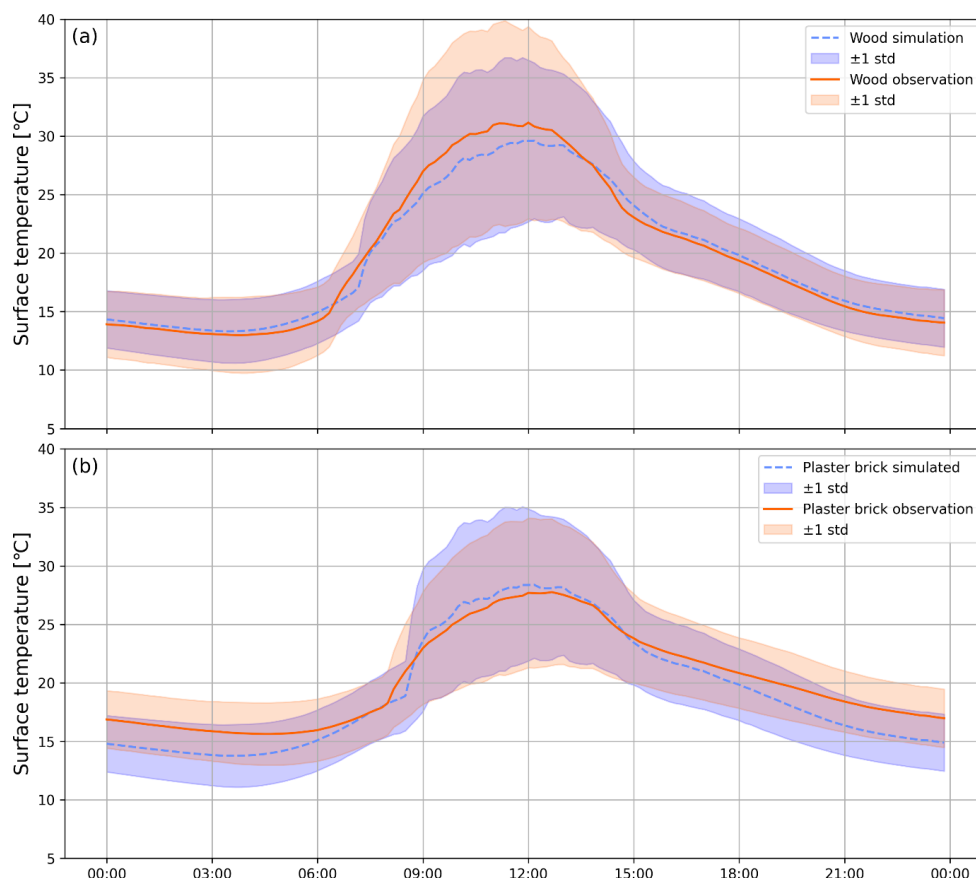
Figure 3: Plots showing wall surface temperatures from 2023-05-15 through to 2023-08-31 (107 days) for (a) the wooden wall and (b) the plaster brick wall. The dashed and solid lines show mean simulated and observed wall surface temperatures, respectively.

230 Scatter plots of 10-minute simulated and observed T_s of the wooden wall, classified into five classes of incoming global shortwave radiation are presented in figures 4a-e, with all values given in figure 4f. The five classes are $K_\downarrow$ < 150 Wm^{-2} (9 days), 150-300 Wm^{-2} (14 days), 300-450 Wm^{-2}, (14 days), 450-600 Wm^{-2} (19 days) and $K_\downarrow$ > 600 Wm^{-2} (51 days), and are based on mean incoming global shortwave radiation ($K_\downarrow$) between 11:00 – 14:00. That is, an entire day will be classified into $K_\downarrow$ < 150 Wm^{-2} if the mean global shortwave radiation between 11:00 –

235 14:00 on this day is below 150 Wm^{-2}.

The first class ($K_\downarrow$ < 150 Wm^{-2}) (figure 4a) shows high correlation between simulations and observations (R^2 = 0.93) and low deviation of simulations (RMSE 1.18 °C). The three following classes (figures 4b-d) have lower

correlations, partly because days in these classes are subject to more cloudy weather, compared to the first class that is subject to overcast conditions. The last class (figure 4e) shows higher agreement between simulations and observations ($R^2 = 0.95$). Overall, with 15,394 observation points (figure 4f), the simulations for the wooden wall correlate well with observed values ($R^2 = 0.93$) and show relatively low RMSE (2.09 °C), indicating that the model performs well.
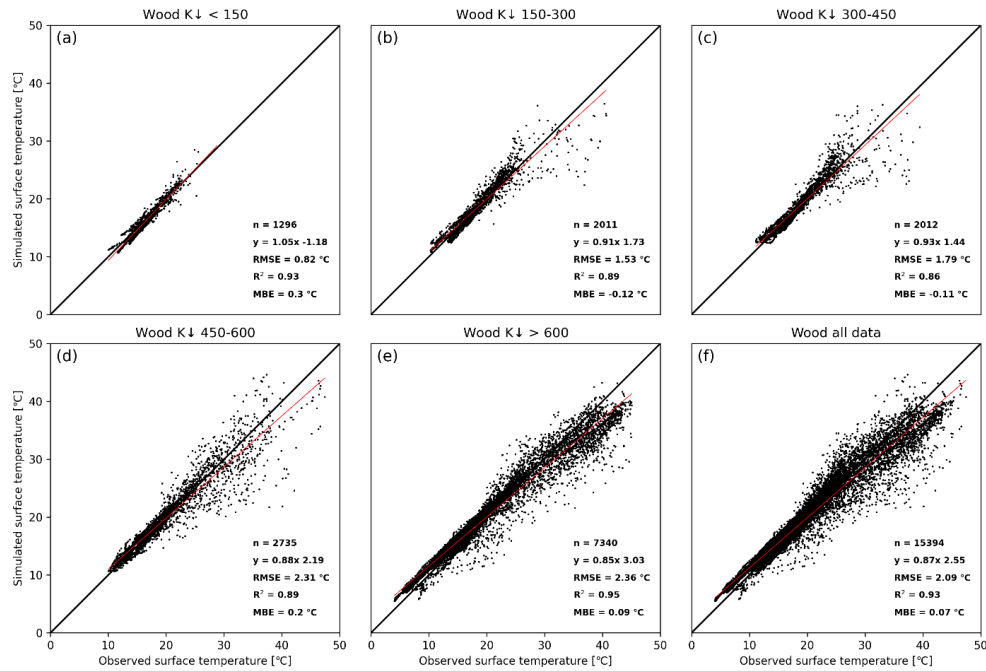
Figure 4: Scatter plots of 10-minute simulated and observed T_s of the wooden wall, classified according to average incoming global shortwave radiation between 11:00 – 14:00 of (a) $K_\downarrow < 150$ Wm^{-2}, (b) 150-300 Wm^{-2}, (c) 300-450 Wm^{-2}, (d) 450-600 Wm^{-2}, (e) > 600 Wm^{-2}, and (f) all data.

Similar scatter plots to those in figure 4, but for the plaster brick wall, are presented in figure 5. Correlations are generally good for all five classes. Best agreement can be seen in $K_\downarrow > 600$ Wm^{-2} ($R^2 = 0.95$) (figure 5e), whereas lowest is evident in $K_\downarrow < 150$ Wm^{-2} (figure 5a) and $K_\downarrow$ 300-450 Wm^{-2} (figure 5c) classes with $R^2 = 0.86$. Highest deviation is found in $K_\downarrow$ 450-600 Wm^{-2} (RMSE = 2.09 °C) (figure 5d), whereas lowest deviation is evident for $K_\downarrow < 150$ Wm^{-2} (RMSE = 1.46 °C) (figure 5a), which can be explained by low incoming shortwave radiation during overcast weather conditions, resulting in a T_s of the wall that is possibly close to T_{air}. All observations combined (figure 5f), simulated T_s show good agreement with observations ($R^2 = 0.94$) and small deviations (RMSE = 1.94 °C).
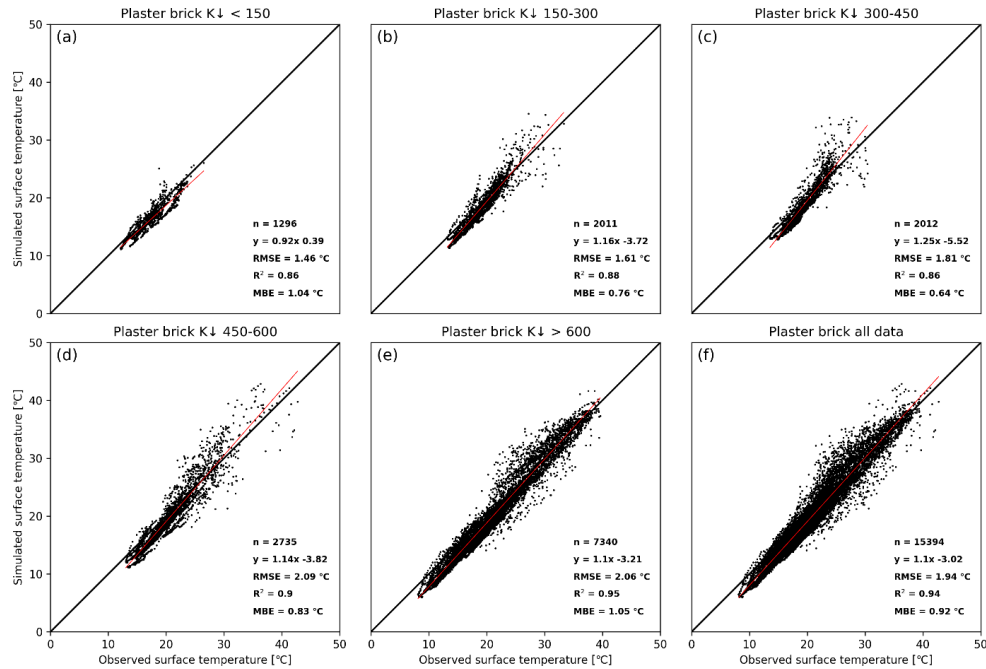
Figure 5: Scatter plots of 10-minute simulated and observed T_s for the plaster brick wall, classified as for Figure 4 into (a) $K_\downarrow$ < 150 Wm⁻², (b) 150-300 Wm⁻², (c) 300-450 Wm⁻², (d) 450-600 Wm⁻², (e) > 600 Wm⁻², and (f) all data.

Comparisons in T_{mrt} at different timesteps are presented in figure 6 to assess the effect of the new parameterization scheme for wall T_s with the previous method (Lindberg et al., 2008). The simulations are for 2023-06-12 (as shown in Figure 2) and the different timesteps compared are (a) 00:00, (b) 03:00, (c) 06:00, (d) 09:00, (e) 12:00, (f) 15:00, (g) 18:00 and (h) 21:00.

The effect of the new scheme on nighttime T_{mrt} in the courtyard is small but noticeable, around 0.3 °C lower compared to the old version (v2022a) of SOLWEIG (figures 6a-b). At 06:00 in the morning (Figure 6c), when the sun is above the horizon but still at a low elevation, more differences in T_{mrt} appear, with some areas having slightly higher values (0.4 °C), while others have slightly lower (–0.2 °C). At 09:00 (figure 6d), more pronounced differences appear, with areas close to the northwestern corner of the courtyard being up to 2.5 °C warmer compared to SOLWEIG v2022a. Here, the sun reaches most of the areas in this corner as the sun is in the east at around 35° elevation, meaning that the direct shortwave component is close to perpendicular to the walls, resulting in high amounts of radiation reaching these surfaces. This becomes evident when looking at the differences for 12:00 (figure 6e), when incoming shortwave radiation is higher but differences are smaller, as this is close to solar noon (~55°) and therefore far from perpendicular to the wall. Nevertheless, differences are about 2.0 °C. At 15:00 when the sun is in the southwest, differences are up to 1.5-2.0 C in the northeastern corner (figure 6f). Here, it is also evident that parts of the walls are shaded by the trees in this corner, which results in lower T_{mrt} (up to around -1.5 °C). When the sun is located in the west ($\theta \approx 270°$) at 18:00, parts of the southeastern corner are sunlit. This results in around 1.0 °C higher T_{mrt} with the new scheme, compared to the old one. In the last example (21:00), T_{mrt} is lower, around -0.6 °C, compared with the old scheme. The sun is close to setting, at an elevation around 5-6°. Thus, the courtyard and its walls are shaded.
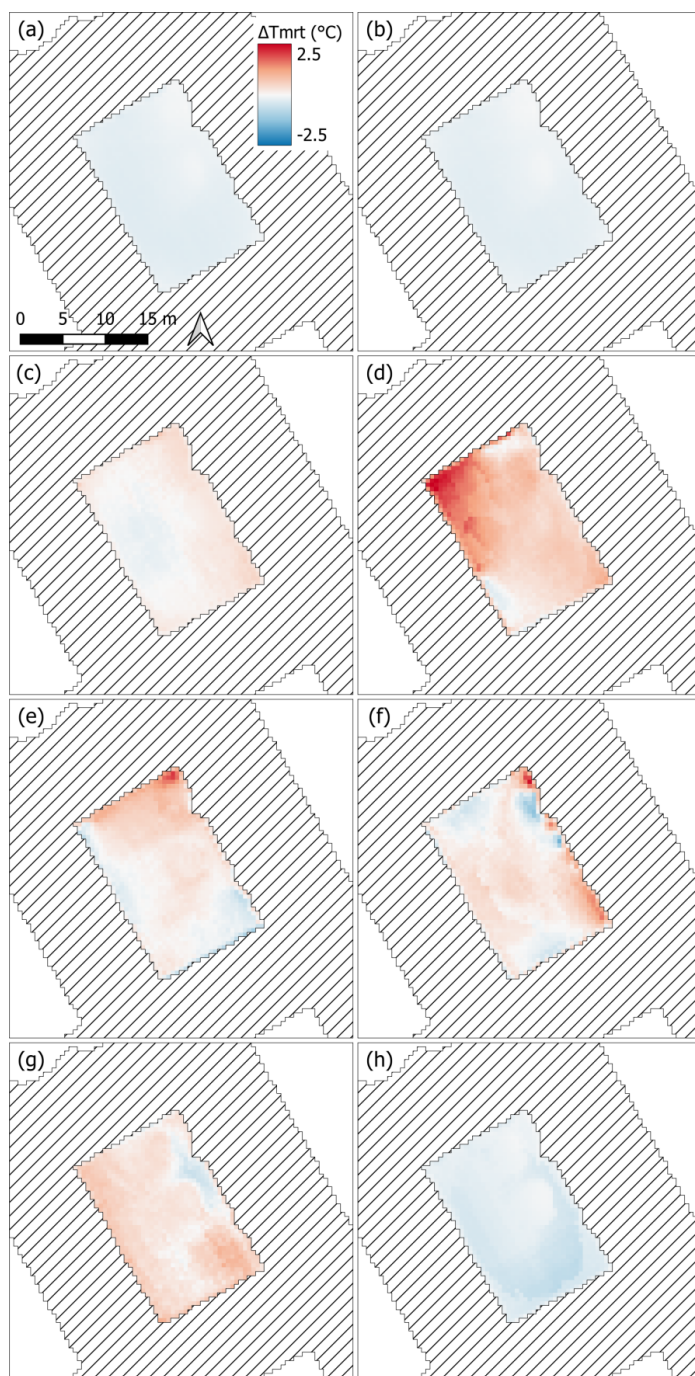
Figure 6: Difference in mean radiant temperature (T_{mrt}) for SOLWEIG simulations with the new and old parameterizations for wall surface temperatures at (a) 2023-06-12 00:00, (b) 03:00, (c) 06:00, (d) 09:00, (e) 12:00, (f) 15:00, (g) 18:00 and (h) 21:00.

280

Since the new wall temperature scheme presented here enables calculation of the variation in T_s at different heights, visualization in 3D provides important information on the distribution of T_s throughout the model domain. As an example, Figure 7 presents a 3D visualization of the surface model used in SOLWEIG (Figure 7a) and wall

285   T_s in central Gothenburg on 2023-06-12 17:00 UTC+1 (Figure 7b). The shadow-casting algorithm in SOLWEIG captures shadows from trees, which are visible along the wall in the top right of the figure. In this area, lower wall temperatures (blue) in shade can be observed, contrasting with the sunlit parts of the wall.
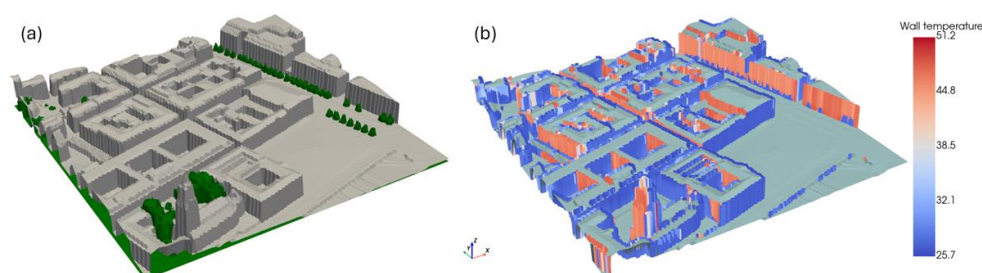
Figure 7: 3D visualization of the (a) digital surface model (DSM) in grey and canopy digital surface model (CDSM) in
290   **green, in the area around Gustaf Adolfs Torg in central Gothenburg, and (b) simulated wall temperatures for the same area. The simulation is for 2023-06-12 17:00:00 UTC+1. Pixel and voxel size is 1 meter. Produced with PyVista (Sullivan et al., 2019).**

4 Discussion

A new and simple method for simulations of wall T_s has been presented. This new parameterization scheme, based
295   on the works of Boue & Fournier (2009), enables estimations of wall T_s for individual vertical pixels described as voxels. This can be compared to the previous method where wall T_s was estimated for either sunlit or shaded façades (Lindberg et al., 2008).

The five-day examples presented in Figure 2 showcase that simulations follow observations. High agreement between simulations and observations is also evident from the statistics in figures 4 and 5, even though correlations
300   decrease with cloudiness, i.e. neither overcast nor clear weather conditions. The lower correlations under cloudy conditions are easily explained by the fact that the SOLWEIG model does not solve for clouds but depends on observations of shortwave radiation, and that observations are from a weather station located approximately 2.3 km from the wall. Nevertheless, R^2 values are high (0.93 and 0.94 for wood and plaster brick respectively), and based on 15,394 observation points, covering the entire summer of 2023. RMSE are also low (2.09 and 1.94 °C).
305   These can be compared to RMSE values for simulated T_s of walls on traditional (3.3 °C) and contemporary (7.4 °C) buildings in Dejvice, Prague, Czech Republic, with the PALM-4U model (Resler et al., 2021) and the T_s simulated with the ENVI-met model for a brick wall covered with plaster (R^2=0.98-0.99, RMSE=1.03-1.25) (Simon, 2016). The better performance of the ENVI-met simulations compared to our method could potentially be explained by the fact that i) ENVI-met make use of a 7-node conduction model and ii) their observations are
310   for a controlled building test site, whereas our results are from a real-world example where we have less knowledge of the thermal properties of the walls. The temperature range for the wooden wall is larger than that of the plaster brick wall, which could be explained by the material characteristics. The wooden wall has a lower thermal effusivity compared to the plaster brick wall, meaning that the wooden wall is more sensitive to changes

in radiation. Thus, the T_s of the wooden wall will fluctuate more, especially during cloudy conditions. The lower
315   thermal effusivity also explains why the T_s of the wooden wall is higher compared to the plaster brick wall.

The present simulation of wall T_s may look simple since there are only two variables involved (T_{air} and net radiation of the wall). However, there are several steps to get the net radiation of the wall. The shortwave radiation depends on the angle between the direct solar radiation and the wall but also reflected radiation from the surrounding surfaces and shadow patterns. The estimation of the outgoing longwave radiation is problematic since
320   it requires information on T_s of the wall, i.e. the variable we want to simulate. As a proxy we use an iterative process starting with the T_s from the previous timestep. Already after the first iteration the wall T_s is stabilized within a few tenths of a degree, which we consider to be close enough to calculate the outgoing longwave radiation.

The wall surface energy balance is of course not only influenced by the net radiation but also by the sensible heat
325   flux to/from the air and the heat flow within the wall. Both these processes are forced by the wall T_s. However, the close connection between the observed and simulated T_s in our study shows that net radiation dominates heating and cooling of the wall surfaces. A similar conclusion was made by Resler et al. (2021). They found it striking that the agreement was better between observed and modelled wall T_s during summer episodes with strong radiative forcing. However, the observed wall T_s of plastered brick walls both in our study and in the study by
330   Resler et al. (2021) were higher than the simulated after the daytime maximum, which indicates an influence of heat stored in the wall earlier during the day. Higher observed than simulated minimum wall T_s, as also noted by Resler et al. (2021), point to an addition of stored heat to the wall surface. On the other hand, the thinner wooden wall with less ability to store heat was cooler than the simulation during the night.

The new parameterization scheme has enabled better estimations of wall T_s and introduced estimations of shading
335   on walls from surrounding buildings and trees (e.g. Figure 7b). This results in differences in T_{mrt} between this new version and previous versions of SOLWEIG. Some of these differences are presented in figure 6 and show that the location of the sun has an effect on T_{mrt}. This is explained by the estimation of wall T_s for individual voxels, where each voxel has its own relation to the location of the sun because of its material characteristics (thermal effusivity, albedo, emissivity) but not the least its aspect. The aspect of the wall, i.e. its orientation, influences
340   how much of the direct shortwave radiation that it is exposed to. Previous studies have concluded that the old parameterization in SOLWEIG led to deviations in simulated wall T_s that affected T_{mrt} (Gal & Kantor, 2020; Wallenberg et al., 2023).

Gal and Kantor (2020), using SOLWEIG, saw deviations in simulated T_{mrt} in proximity to wall surfaces and suggested a separate surface temperature parameterization scheme. Some of the overestimations were potentially
345   reduced by around 3 °C with the introduction of patches for short- and longwave radiation described in Wallenberg et al. (2020; 2023a). The new parameterization scheme for wall T_s should improve these deviations further. For example, underestimations were seen in vicinity of sunlit areas (Gal & Kantor, 2020). Here, we show (e.g. Figure 6d) that the new wall surface scheme calculates higher T_{mrt} close to sunlit walls (up to 2.5 °C for our case). A small decrease is also noticeable under the trees (Figure 6f-g). These differences come from the directionality of
350   the walls and accounting for whether they are sunlit or shaded, which was previously not possible.

Kim & Ham (2024) found deviations in simulated T_s of asphalt, plywood and soil, and suggested improvements in thermophysical attributes of construction materials in calculations in SOLWEIG. Although their study referred to horizontal surfaces (e.g. ground and roofs) the suggestions are in line with what has been presented in this paper. The old parameterization scheme for wall T_s is based on the parameterization scheme for ground surface

355   temperatures utilized in SOLWEIG. This scheme was initially developed by Bogren et al. (2000) and refined by Lindberg et al. (2016) and is based on a sinusoidal curve that peaks at a set time. For ground surfaces, this peak in time might be accurate as it occurs not long after solar noon. For walls, however, one peak time for the entire model domain will lead to differences in T_s, depending on the aspect of the wall. Peak time of a wall facing east will for example occur in the morning, whereas it will occur in the afternoon or evening for a wall facing west.

360   The T_s scheme presented here, thus, is an improvement in SOLWEIG, but for wall surfaces. The method presented could, however, be useful for ground surfaces as well and is an expected future effort.

Even though the model performs well, there are some shortcomings. For example, the spatial input data is pixel based. This leads to deviations when estimating wall aspects. Although the accuracy of aspect calculations is high in mid-sections of the walls, deviations occur close to corners. Other potential sources of error could be the

365   material characteristics used here, i.e. thermal conductivity, specific heat capacity, density, wall thickness, emissivity and albedo.

The new scheme has only introduced four new input parameters to the SOLWEIG model: thermal conductivity, density, specific heat capacity and thickness of the wall. These parameters are easily accessible in literature (e.g. CIBSE, 2015). Three materials are available in the new publicly available SOLWEIG model: brick, concrete and

370   wood. Other materials can simply be added to the parameter file in SOLWEIG. One drawback with the new scheme is the computational speed. Running the model for one day at 10-minute resolution (144 time steps) took approximately 5 minutes with the newly implemented wall scheme parameterization, compared to around 1 minute without it, on an Intel i7-7700 CPU @ 3.6 GHz with 16 GB RAM. However, this is still faster than most other models designed for similar purposes.

375   Future efforts include improvement of the ground surface calculations, possibly by introducing the methods presented here. Moreover, the parameterization scheme should be evaluated for other wall surfaces and urban environments, as well as a deeper evaluation of the behavior of walls and their influence of microclimate.

5 Conclusions

We have presented a new parameterization scheme for calculations of wall T_s. The scheme is simple and fast,

380   with only four new input parameters: thermal conductivity, density, specific heat capacity and wall thickness, together with a heat flux density, in this case the heat balance of the wall surface. The performance of the scheme is high for the two assessed wall surfaces, wood ($R^2 = 0.93$, RMSE = 2.09 °C) and plaster brick ($R^2 = 0.94$, RMSE = 1.94 °C), making it comparable to heat conductivity models utilized in other models for microclimate.

The implementation of the scheme in the SOLWEIG model has enabled more realistic estimations of wall T_s by

385   incorporating wall aspects and material characteristics. In the examples presented here this has led to differences in T_{mrt} of up to 2.5 °C compared to the previous version of SOLWEIG.

With this new scheme SOLWEIG can now be used to understand how different building materials influence outdoor thermal comfort. The high accuracy indicated by our results combined with the computational speed suggests that this approach can be used in other areas where T_s of walls are important, for example building energy and urban energy balance models.

The new version of SOLWEIG presented here and its associated datasets are available in Wallenberg et al. (2025a; b).

Code availability

The mode code is available from https://doi.org/10.5281/zenodo.15309383 (Wallenberg et al., 2025a). A dataset consisting of required forcing data for SOLWEIG (DEM, DSM, CDSM, ground cover, meteorological data) and observed and simulated wall surface temperatures used in the study are available from https://doi.org/10.5281/zenodo.15309444.

Author contributions

NW developed the model code (Software) and performed the simulations (Formal analysis). NW, FL, and JL prepared and conducted the field campaign (Investigation). NW prepared the manuscript (Writing – original draft) with contributions from all co-authors (Writing – review & editing). EM and DL formulated the initial model design (Conceptualization), and NW, BH, FL, and JL finalized the model (Methodology).

Competing interests

The authors declare that they have no conflict of interest.

References

Adilkhanova, I., Santamouris, M., and Yun, G. Y.: Coupling urban climate modeling and city-scale building energy simulations with the statistical analysis: Climate and energy implications of high albedo materials in Seoul, Energy Build., 290, https://doi.org/10.1016/j.enbuild.2023.113092, 2023.

Ali-Toudert, F., and Mayer, H.: Numerical study on the effects of aspect ratio and orientation of an urban street canyon on outdoor thermal comfort in hot an dry climate, Building and Environment, 41, 94-108, https://doi.org/10.1016/j.buildenv.2005.01.013, 2005.

Apogee Instruments: Infrared radiometers SI-100 Series, SIF-100 Series, SI-400 Series, SIL-100 Series, & SIL-400 Series, Apogee Instruments, Logan, UT, https://www.apogeeinstruments.com/content/SI-100-400-spec-sheet.pdf, 2024.

Arnfield, A. J.: Two decades of urban climate research: A review of turbulence, exchanges of energy and water, and the urban heat island, Int. J. Climatol., 23, 1–26, https://doi.org/10.1002/joc.859, 2003.

Battista, G., de Lieto Vollaro, E., Ocłoń, P., and de Lieto Vollaro, R.: Effects of urban heat island mitigation strategies in an urban square: A numerical modelling and experimental investigation, Energy Build., 282, https://doi.org/10.1016/j.enbuild.2023.112809, 2023.

420 Blazejczyk, K., Broede, P., Fiala, D., Havenith, G., Holmér, I., Jendritzky, G., Kampmann, B., and Kunert, A.: Principles of the new universal thermal comfort index (UTCI) and its application to bioclimatic research in European scale, Misc. Geogr., 14(1), 91–102, https://doi.org/10.2478/mgrsd-2010-0009, 2010.

Bogren, J., Gustavsson, T., Karlsson, M., and Postgård, U.: The impact of screening on road surface temperature, Meteorol. Appl., 7, 97–104, https://doi.org/10.1017/S135048270000150X, 2000.

425 Boué, C. and Fournier, D.: Infrared thermography measurements of the thermal parameters (effusivity, diffusivity and conductivity) of materials. Quant. InfraRed Thermog. J., 6:2, 175-188, https://doi.org/10.3166/qirt.6.175-188, 2008.

Bruse, M., and Fleer, H.: Simulating surface–plant–air interactions inside urban environments with a three-dimensional numerical model, Environ. Model. Softw., 13(3), 373-384, https://doi.org/10.1016/S1364-430 8152(98)00042-5, 1998.

Bäcklin, O., Lindberg, F., Thorsson, S., Rayner, D., and Wallenberg, N.: Outdoor heat stress at preschools during an extreme summer in Gothenburg, Sweden – Prescohool teachers' experiences contextualized by radiation modelling, Sustain. Cities and Soc., 75, 103324, https://doi.org/10.1016/j.scs.2021.103324, 2021.

Cape, J.A., and Lehman, G.W.: Temperature and Finite Pulse-Time Effects in the Flash Method for Measuring 435 Thermal Diffusivity, J. Appl. Phys., 34, 1909-1913, https://doi.org/10.1063/1.1729711, 1963.

Celniker, C., Chen, S. A., Meier, A., and Levinson, R.: Targeting buildings for energy-saving cool-wall retrofits: a case study at the University of California, Davis, Energy Build., 249, 111014, https://doi.org/10.1016/j.enbuild.2021.111014, 2021.

CIBSE, Guide A Environmental design, Chartered Institution of Building Services Engineers, UK, ISBN 440 9781906846541, 2015.

Di Napoli, C., Hogan, R. J., and Pappenberger, F.: Mean radiant temperature from global-scale numerical weather prediction models, Int. J. Biometeorol., 64(7), 1233-1245, https://doi.org/10.1007/s00484-020-01900-5, 2020.

Gál, C.V. and Kántor, N.: Modeling mean radiant temperature in outdoor spaces, A comparative numerical simulation and validation study, Urban Climate, 32, 100571, https://doi.org/10.1016/j.uclim.2019.100571, 2020.

445 Höppe, P.: A new procedure to determine the mean radiant temperature outdoors, Wetter Leben, 44, 147–151, 1992.

Höppe, P.: The physiological equivalent temperature – a universal index for the biometeorological assessment of the thermal environment, Int. J. Biometeorol., 43, 71–75, https://doi.org/10.1007/s004840050118, 1999.

Kantor, N., Gal, CV., Gulyas, A., and Unger, J.: The impact of façade orientation and woody vegetation on
450   summertime heat stress patterns in a central European square: comparison of radiation measurements and
simulations, Adv. Meteorol. 2018, 2650642, https://doi.org/10.1155/2018/2650642, 2018.

Kim, Y and Ham, Y.: Spatio-temporal heat risk analysis in construction: Digital twin-enabled monitoring,
Automation in Construction, 168, Part A, 105805, https://doi.org/10.1016/j.autcon.2024.105805, 2024.

Lau, K. K., et al.: The effect of urban geometry on mean radiant temperature under future climate change: A study
455   of three European cities, Int. J. Biometeorol., 59(7), 799-814, https://doi.org/10.1007/s00484-014-0898-1, 2015.

Lindberg, F. and Grimmond, C. S. B.: Nature of vegetation and building morphology characteristics across a city:
influence on shadow patterns and mean radiant temperature in London, Urban Ecosyst., 14, 617–634,
https://doi.org/10.1007/s11252-011-0184-5, 2011a.

Lindberg, F. and Grimmond, C. S. B.: The influence of vegetation and building morphology on shadow patterns
460   and mean radiant temperature in urban areas: Model development and evaluation, Theor. Appl. Climatol., 105,
311–323, https://doi.org/10.1007/s00704-010-0382-8, 2011b.

Lindberg, F., Holmer, B., and Thorsson, S.: SOLWEIG 1.0 – modelling spatial variations of 3D radiation fluxes
and mean radiant temperature in complex urban settings, Int. J. Biometeorol., 52, 697–713,
https://doi.org/10.1007/s00484-008-0162-7, 2009.

465   Lindberg, F., Holmer, B., Thorsson, S., and Rayner, D.: Characteristics of the mean radiant temperature in high
latitude cities – implications for sensitive climate planning applications, Int. J. Biometeorol., 58, 613–627,
https://doi.org/10.1007/s00484-013-0638-y, 2013.

Lindberg, F., Onomura, S., and Grimmond, C. S. B.: Influence of ground surface characteristics on the mean
radiant temperature in urban areas, Int. J. Biometeorol., 60(9), 1439–1452, https://doi.org/10.1007/s00484-016-
470   1135-x, 2016.

Lindberg, F., Grimmond, C. S. B., Gabey, A., Huang, B., Kent, C. W., Sun, T., Theeuwes, N., Järvi, L., Ward,
H., Capel-Timms, I., Chang, Y. V., Jonsson, P., Krave, N., Liu, D., Meyer, D., Olofson, F., Tan, J. G., Wästberg,
D., Xue, L., and Zhang, Z.: Urban Multi-Scale Environmental Predictor (UMEP): An integrated tool for city-
based climate services, Environ. Modell. Softw., 99, 70–87, https://doi.org/10.1016/j.envsoft.2017.09.020, 2018.

475   Maronga, B., Banzhaf, S., Burmeister, C., Esch, T., Forkel, R., Fröhlich, D., Fuka, V., Gehrke, K.F., Geletič, J.,
Giersch, S., Gronemeier, T., Groß, G., Heldens, W., Hellsten, A., Hoffmann, F., Inagaki, A., Kadasch, E., Kanani-
Sühring, F., Ketelsen, K., Khan, B.A., Knigge, C., Knoop, H., Krč, P., Kurppa, M., Maamari, H., Matzarakis, A.,
Mauder, M., Pallasch, M., Pavlik, D., Pfafferott, J., Resler, J., Rissmann, S., Russo, E., Salim, M., Schrempf, M.,
Schwenkel, J., Seckmeyer, G., Schubert, S., Sühring, M., von Tils, R., Vollmer, L., Ward, S., Witha, B., Wurps,
480   H., Zeidler, J., and Raasch, S.: Overview of the PALM model system 6.0, Geosci. Model Dev., 13, 1335–1372,
https://doi.org/10.5194/gmd-13-1335-2020, 2020.

Matzarakis, A., Rutz, F., and Mayer, H.: Modelling radiation fluxes in simple and complex environments—
application of the RayMan model, Int. J. Biometeorol., 51(4), 323-334, https://doi.org/10.1007/s00484-006-0061-
8, 2007.

485   Matzarakis, A., Rutz, F., and Mayer, H.: Modelling radiation fluxes in simple and complex environments: basics
        of the RayMan model, Int. J. Biometeorol., 54(2), 131-139, https://doi.org/10.1007/s00484-009-0261-0, 2010.

        Muniz-Gäal, L. P., Pezzuto, C. C., Carvalho, M. F. H. d., and Mota, L. T. M.: Urban geometry and the
        microclimate   of   street   canyons   in   tropical   climate,   Build.   Environ.,   169,
        https://doi.org/10.1016/j.buildenv.2019.106547, 2020.

490   Nasrollahi, N., Namazi, Y., and Taleghani, M.: The effect of urban shading and canyon geometry on outdoor
        thermal comfort in hot climates: A case study of Ahvaz, Iran, Sustain. Cities Soc., 65,
        https://doi.org/10.1016/j.scs.2020.102638, 2021.Parker, W.J., Jenkins, R.J., Butler, C.P., and Abbott, G.L.: Flash
        Method for Determining Thermal Diffusivity, Heat Capacity and Thermal Conductivity, J. Appl. Phys., 32, 1679-
        1684, https://doi.org/10.1063/1.1728417, 1961.

495   Philipp, A., Eichinger, J.F., Aydin, R.C., Georgiadis, A., Cyron, C.J., and Retsch, M.: The accuracy of laser flash
        analysis explored by finite element method and numerical fitting, Heat and Mass Transfer, 56, 811-823,
        https://doi.org/10.1007/s00231-019-02742-7, 2020.

        Prata, A. J.: A new long-wave formula for estimating downward clear-sky radiation at the surface, Q. J. R.
        Meteorol. Soc., 122, 1127–1151, https://doi.org/10.1002/qj.49712253306, 1996.

500   Ratti, C. and Richens, P.: Raster analysis of urban form, Environ. Plann. B: Urban Ana. City Sci., 31, 297–309,
        https://doi.org/10.1068/b2665, 2004.

        Resler, J., Krc, P., Belda, M., Jurus, P., Benesova, N., Lopata, J., Vlcek, O., Damaskova, D., Eben, K., Derbek,
        P., Maronga, B., and Kanani-Sühring, F.: PALM-USM v1.0: A new urban surface model integrated into the
        PALM large-eddy simulation model, Geosci. Model Dev., 10, 3636-3659, https://doi.org/10.5194/gmd-10-3635-
505   2017, 2017.

        Resler, J., Eben, K., Geletic, J., Krc, P., Rosecky, M., Sühring, M., Belda, M., Fuka, V., Halenka, T., Huszar, P.,
        Karlicky, J., Benesova, N., Doubalova, J., Honzakova, K., Keder, J., Napravnikova, S., and Vlcek, O.: Validation
        of the PALM model system 6.0 in a real urban environment: a case study in Dejvice, Prague, the Czech Republic,
        Geosci. Model Dev., 14, 4797-4842, https://doi.org/10.5194/gmd-14-4797-2021, 2021.

510   Santamouris, M., and Yun, G. Y.: Recent development and research priorities on cool and super cool materials to
        mitigate urban heat island, Renew. Energy, 161, 792-807, https://doi.org/10.1016/j.renene.2020.07.109, 2020.

        Schibuola, L., and Tambani, C.: A monthly performance comparison of green infrastructures enhancing urban
        outdoor thermal comfort, Energy Build., 273, https://doi.org/10.1016/j.enbuild.2022.112368, 2022.

        Simon, H.: Modeling urban microclimate: Development, implementation and evaluation of new and improved
515   calculation methods for the urban microclimate model ENVI-met, Dissertation zur Erlangung des Grades "Doktor
        der Naturwissenschaften" im Promotionsfach Geographie am Fachbereich Chemie, Pharmazie und
        Geowissenschaften der Johannes Gutenberg-Universität Mainz, Mainz, März 2016.

Stache, E., Schilperoort, B., Ottelé, M., and Jonkers, H. M.: Comparative analysis in thermal behaviour of common urban building materials and vegetation and consequences for urban heat island effect, Build. Environ., 520   213, https://doi.org/10.1016/j.buildenv.2021.108489, 2022.

Sullivan, C., Kaszynski, A., and Panetta, J.: PyVista: 3D plotting and mesh analysis through a streamlined interface for the Visualization Toolkit (VTK), J. Open Source Softw., 4(37), 1450, https://doi.org/10.21105/joss.01450, 2019.

Tinytag: Tinytag Plus 2 Dual Channel Temperature/Relative Humidity (-25 to +85 C/0 to 100% RH), TGP-4500, 525   Data sheet, Issue 13, Gemini Data Loggers, https://assets.geminidataloggers.com/pdfs/original/3751-tgp-4500.pdf, 2019.

Thom, J., Coutts, A. M., Broadbent, A. M., and Tapper, N. J.: The influence of increasing tree cover on mean radiant temperature across a mixed development suburb in Adelaide, Australia, Urban Forest. Urban Green., 20, 233–242, https://doi.org/10.1016/j.ufug.2016.08.016, 2016.

530   Thorsson, S., Lindberg, F., Eliasson, I., and Holmer, B.: Different methods for estimating the mean radiant temperature in an outdoor urban setting, Int. J. Climatol., 27, 1983–1993, https://doi.org/10.1002/joc.1537, 2007.

Wallenberg, N., Lindberg, F., Holmer, B., and Thorsson, S.: The influence of anisotropic diffuse shortwave radiation on mean radiant temperature in outdoor urban environments, Urban Climate, 31, 100589, https://doi.org/10.1016/j.uclim.2020.100589, 2020.

535   Wallenberg, N., Holmer, B., Lindberg, F., Rayner, D.: An anisotropic parameterization scheme for longwave irradiance and its impact on radiant load in urban outdoor settings, Int. J. Biometeorol. 67, 633-647, https://doi.org/10.1007/s00484-023-02441-3, 2023a.

Wallenberg, N., Lindberg, F., Thorsson, S., Jungmalm, J., Fröberg, A., Raustorp, A., and Rayner, D.: The effects of warm weather on children's outdoor heat stress and physical activity in a preschool yard in Gothenburg, 540   Sweden, Int. J. Biometeorol., 67, 1927-1940, https://doi.org/10.1007/s00484-023-02551-y, 2023b.

Wallenberg, N., Lindberg, F., Holmer, B., and Lönn, J. SOLWEIG v2025 as part of UMEP-processing, Zenodo [code], https://doi.org/10.5281/zenodo.15309383, 2025a.

Wallenberg, N., Lindberg, F., Holmer, B., and Lönn, J. SOLWEIG v2025 test dataset, Zenodo [data set], https://doi.org/10.5281/zenodo.15309444, 2025b.

545   Xi, C., Ren, C., Wang, J., Feng, Z., and Cao, S.: Impacts of urban-scale building height diversity on urban climates: A case study of Nanjing, China, Energy Build., 251, https://doi.org/10.1016/j.enbuild.2021.111350, 2021.

Xue, J., Liu, X., Lian, Y., and Taylor, R.: The Effects of a Finite Pulse Time in the Flash Thermal Diffusivity Method, Int. J. Thermophys. 14(1), 123-133, https://doi.org/10.1007/BF00522666, 1993.